ASIA-PACIFIC JOURNAL OF CHEMICAL ENGINEERING
Asia-Pac. J. Chem. Eng. (2014)
Published online in Wiley Online Library
(wileyonlinelibrary.com) DOI: 10.1002/apj.1791

Research article

Comparison of preparation methods for iron–alumina oxygen carrier and its reduction kinetics with hydrogen in chemical looping combustion

Haibo Zhao, Daofeng Mei, Jinchen Ma and Chuguang Zheng*

State Key Laboratory of Coal Combustion, Huazhong University of Science and Technology, Wuhan 430074, P.R. China

Received 28 November 2013; Revised 20 January 2014; Accepted 21 January 2014

ABSTRACT: Seven preparation methods, namely sol-gel, co-precipitation, hydrothermal synthesis, low heating solid-state reaction, freeze granulation, combustion synthesis, and mechanical mixing, were used to synthesize Fe_2O_3/Al_2O_3 oxygen carrier for chemical looping combustion. A comprehensive physicochemical characterization (i.e. productivity, crushing strength, crystalline characteristics, microstructure, and chemical reactivity with hydrogen) was carried out, and the effects of preparation methods and processes on the oxygen carrier performance were explored. Taking into consideration various physicochemical indices, the sol-gel method and the freeze granulation method were preferred for oxygen carrier preparation. Following that, a critical chemical reaction in *in situ* gasification chemical looping combustion, the reduction reaction between oxygen carrier and hydrogen, was clarified in terms of reaction kinetics through the non-isothermal kinetics analysis and the double extrapolation method. Temperature programmed reduction experiments of the sol-gel-derived Fe_2O_3/Al_2O_3 particle and hydrogen were performed using a chemisorption analyzer. The reduction mechanisms and kinetics parameters for the two-stage reaction (reduced from Fe_2O_3 to Fe_3O_4 and then from Fe_3O_4 to $FeAl_2O_4$) were determined. In the first stage, the reduction reaction is described by the surface reaction model with an order of 2; on the other hand, the conversion from Fe_3O_4 to $FeAl_2O_4$ is dominated by the nucleation and nuclei growth process. © 2014 Curtin University of Technology and John Wiley & Sons, Ltd.

KEYWORDS: chemical looping combustion; oxygen carrier; kinetics mechanism; sol-gel; freeze granulation

INTRODUCTION

Chemical looping combustion (CLC) is one of the most promising technologies to concentrate and separate CO_2 from the combustion of fossil fuel (e.g. coal). Chemical looping technology is based on the cyclic reduction–oxidation reaction of metal oxide or other compound, named oxygen carrier (OC). The role of OC is to transfer active oxygen from air to fuel, avoiding direct contact between fuel and air. The new carbon capture technology allows a sequestration-ready CO_2 stream to be directly generated from a two-step reaction. There are two reactors, air reactor (AR) and fuel reactor (FR), in a CLC system. Solid-state OC particles circulate between the FR and the AR. Once entering into the FR, OCs with high oxygen potential (MeO_x) react with the fuel in the FR and are reduced to the low-valence oxides (MeO_{x-1}), which are then re-oxidized backed to MeO_x in the AR. The exhaust from the FR contains mainly steam and CO_2, from which pure CO_2 stream can be obtained after condensation. Thus, the CLC technology is a low energy penalty approach for CO_2 capture.

Normally, Al_2O_3, TiO_2, SiO_2, ZrO_2, kaolin, sepiolite, bentonite, yttria-stabilized zirconium, or hexaaluminate was used as an inert support in an OC particle to improve its mechanical strength and attrition resistance. The active component of OC could be Cu-based, Fe-based, Mn-based, Ni-based and Co-based oxide, and $CaSO_4$.[1] The OC was usually synthesized through a well-rounded chemical or physical method on experimental scale. The alternative methods for OC preparation included sol-gel,[2] impregnation,[3–5] co-precipitation,[6–8] hydrothermal synthesis,[9] low heating solid-state reaction,[10] freeze granulation,[11–13] combustion synthesis,[14–16] and mechanical mixing.[17–19] For more details, readers could refer to the two excellent reviews.[20,21] It has been verified that the preparation method has obvious effects on the OC physicochemical properties,[7,9,22] such as chemical reactivity, surface area, pore structure, particle size, mechanical strength, resistance to attrition and fragmentation, resistance to sintering and agglomeration,

**Correspondence to*: Haibo Zhao, State Key Laboratory of Coal Combustion, Huazhong University of Science and Technology, Wuhan 430074, P.R. China. E-mail: klinsmannzhb@163.com

oxygen transport capacity, and even composition distribution. Even if the same preparation method is used, different preparation processes (e.g. with different calcination temperatures and calcination times) may affect the physicochemical properties (e.g. long-term recyclability and durability, thermodynamic characteristics, and even active site distribution) as well. It is thus necessary to classify the effects of the preparation method and the preparation process on the OC performance with regard to a specified OC.

Among different OCs, the iron-based OC has been highlighted by researchers because it is at comprehensive advantages of being economically feasible, environmentally benign, resistant to agglomeration, mechanical resistant to friction stress, stable under multi-oxidation/reduction cycles at high temperature, and moderately reactive. Also, some natural materials mainly consisting of Fe_2O_3 and Al_2O_3, e.g. iron ore, were considered in the CLC process. Therefore, this paper focuses on the synthesized Fe_2O_3/Al_2O_3 OC with a content of 60 wt % Fe_2O_3 and 40 wt% Al_2O_3. Using 40 wt% Al_2O_3 as support has been demonstrated to give stable conversion and good reactivity.[23,24] The OC was prepared through seven methods, namely sol-gel, co-precipitation, hydrothermal synthesis, low heating solid-state reaction, freeze granulation, combustion synthesis, and mechanical mixing, to explore the effect of the preparation techniques on its performance. It is noted that the impregnation method is also an important OC preparation method, which could give highly reactive materials but with a lower active material content.[25]

In the *in situ* gasification chemical looping combustion (iG-CLC), solid fuel (e.g. coal) is first gasified by an agent (steam/CO_2), generating syngas (contains mainly H_2 and CO) *in situ*. The coal-gasification process is a rate-limiting step[26,27] in the iG-CLC, and the inhibition of H_2 in gasification products strongly affects the conversion of char in the FR. The OC can also play a role of removing H_2 by reacting with it, which can thus accelerate the coal gasification and then speed up the iG-CLC process. This suggests that the coal conversion in the iG-CLC can be enhanced by using an OC that can convert H_2 more effectively. The kinetics and mechanism of chemical reactions involved in the iG-CLC are important for the design, operation, performance prediction, and numerical simulation of iG-CLC reactors.[28,29] There are mainly two methods for kinetics determination, named the isothermal method and the non-isothermal method.[30–34] For both methods, many kinds of reaction kinetics models [35–38] can be used to describe the reaction process, such as the nucleation and nuclei growth model, the shrinking core model, the phase-boundary-controlled reaction model, the one/two/three-dimensional diffusion model, the power-law relation model, and the Sestak–Berggren model. For more comprehensive summarization on reaction kinetics, readers can refer to two excellent reviews by Hossain *et al.*[20] and Adánez *et al.*[21] However, the understanding on the reduction kinetics between H_2 and the Fe_2O_3/Al_2O_3 OC is still limited because of the particularity of the iron's valence (mainly Fe^0, Fe^{2+}, $Fe^{8/3+}$, and Fe^{3+}) in the Fe-based OC and the formation of $FeAl_2O_4$ compound during the reduction processes of iron–alumina OC.[24] When iron oxide is reduced to different valences, the reduction mechanism and the kinetics parameters have to be differentiated.

This paper focused on the optimal selection of the preparation techniques for Fe_2O_3/Al_2O_3 OC particles and the investigation of the reduction reaction kinetics and mechanism between the sol-gel-derived Fe_2O_3/Al_2O_3 and hydrogen. The paper was organized as follows. In the section on Oxygen Carrier Preparation, seven methods were introduced to prepare the Fe_2O_3/Al_2O_3 (60 wt%/40 wt%) OC. Four different calcination temperatures and four different calcination durations were selected to investigate the effect of the calcination process on the OC properties. In the section on Comparison and Evaluation of the Preparation Techniques, these OCs were compared and evaluated in terms of productivity, crushing strength, crystalline phase, morphological structure, and chemical reactivity with hydrogen. The optimal preparation techniques for the iron-based OC were then determined through the comprehensive evaluation of the OC physicochemical properties. In the section on Reaction Kinetics of the Sol-gel-derived Fe_2O_3/AL_2O_3 with Hydrogen, the reduction kinetics of the reaction between hydrogen and the optimal OC was further investigated through temperature programmed reduction (TPR) experiments performed in a chemisorption analyzer. Finally, conclusions were given in the last section.

OXYGEN CARRIER PREPARATION

Generally, the OC preparation process can be divided into three subprocesses: the preparation of precursor, the drying and calcination of precursor, and the grinding and sieving of agglomerate. Usually, the precursor drying and calcination and the agglomerate grinding and sieving are common for these preparation methods. The preparation methods differ mainly in the preparation route of the precursor. Sol-gel, co-precipitation, low heat solid reaction, hydrothermal synthesis, mechanical mixing, combustion synthesis, and freeze granulation are usually applied for the precursor preparation. In this study, the OC of 60 wt% Fe_2O_3 loaded on Al_2O_3 was prepared through the seven methods.

DOI: 10.1002/apj

Precursor preparation

Sol-gel

The sol-gel process can be divided into three steps, i.e. the preparation of boehmite γ-AlOOH sol, the preparation of the γ-AlOOH wet gel with $Fe(NO_3)_3$ distribution, and the drying of the wet gel. First of all, the aluminum isopropoxide ($Al(C_3H_7O)_3$, KESHI Co., AR level, 99.9%) was ground and selected as a precursor for the boehmite sol. Then, $Al(C_3H_7O)_3$ (39.98 g) was dissolved in the deionized water, where the molar ratio H_2O/Al^{3+} was 100, and hydrolyzed in a 85 °C water bath for 1.5 h. Following that, a certain amount of HNO_3 (1 mol/L), given the ratio H^+/Al^{3+} of 0.007, was added into the solution. Afterward, the temperature of the water bath was raised to 90 °C, at which the solution was aged for 12 h to obtain the boehmite γ-AlOOH sol. After evaporation for 0.5 h, a certain amount of $Fe(NO_3)_3$ solution (prepared from 75.95 g $Fe(NO_3)_3{\cdot}9H_2O$, Sinopharm Co., AR level, 99.9%) was added to the boehmite sol under the condition of fully stirring. Finally, the generated wet gel was dried in an oven in a step by step manner (80 °C for 24 h, 100 °C for 5 h, 150 °C for 5 h, and 200 °C for 5 h) to obtain the dried precursor.

Co-precipitation

In the deionized water, 75.95 g Fe $(NO_3)_3{\cdot}9H_2O$ (Sinopharm Co., AR level, 99.9%) and 73.53 g Al $(NO_3){\cdot}9H_2O$ (Kermel Co., AR level, 99.9%) were dissolved to obtain a 300-mL mixture solution. Subsequently, 400-mL thick ammonia was slowly dropped into the solution through a peristaltic pump till pH of 9–10, generating a brown precipitation. The turbid liquid was further evaporated to remove the water to obtain a wet powder. It was then dried in an oven at 80 °C for 24 h to obtain the precursor.

Low heat solid reaction

In an agate mortar, 52.27 g $FeSO_4{\cdot}7H_2O$ (Tianjin chemical reagent Co., AR level, 99.9%), 65.31 g $Al_2(SO_4)_3{\cdot}18H_2O$ (Tianjin chemical reagent Co., AR level, 99.9%), and 46.08 g NaOH (Sinopharm Co., AR level, 99.9%) were mixed and ground slowly, in which three agents reacted with each other producing a black intermediate product with a large amount of heat release. After grinding for 0.5 h, the black product was washed and filtrated more than five times through a funnel till no SO^{4-} was detected in the solution (by the titration of $Ba(OH)_2$ solution to observe if the white precipitation $BaSO_4$ is generated). Finally, the washed intermediate was dried in an oven at 80 °C for 12 h and then at 100 °C for 5 h to produce the precursor.

Hydrothermal synthesis

An Fe–Al precipitation was prepared through the same process as that of the co-precipitation technique. The precipitation was then separated from the solution and dispersed into the deionized water and aged at 80 °C for 5 h to gain hydrosol. Then, the hydrosol was mixed with 100 mL of 5% polyvinyl acetate to obtain a wet gel. After cooling down, the gel was introduced into a kettle in which the temperature of 200 °C was maintained for 3 h under the self-generated pressure to synthesize an intermediate. The intermediate was then dried in an oven at 80 °C for 24 h to obtain the precursor.

Mechanical mixing

A total of 15 g Fe_2O_3 (Tianjin Dengfeng Co., AR level, 99.9%) and 10 g Al_2O_3 (Shanghai Wusi Co., AR level, 99.9%) were mixed and ground for 30 min in a mill to obtain a well-dispersed powder. Then, the powder was mixed with 100 mL of 5% polyvinyl acetate to achieve a well-dispersed powder mixture, which was then ground for another 30 min to produce the wet gel. The gel was then dried in an oven at 80 °C for 24 h and at 100 °C for 5 h successively to obtain the precursor.

Combustion synthesis

A total of 75.95 g $Fe(NO_3)_3{\cdot}9H_2O$ (Sinopharm Co., AR level, 99.9%), 73.53 g $Al(NO_3)_3{\cdot}9H_2O$ (Sinopharm Co., AR level, 99.9%), and 11.64 g urea (Sinopharm Co., AR level, 99.9%) were dissolved in the deionized water with full stirring in a water bath at 75 °C for 6 h to evaporate the water and produce a wet gel. The gel was then dried in an oven at 80 °C for 6 h and successively at 120 °C for 6 h to produce a dried gel. The gel was then heated to 600 °C in a muffle furnace and ignited to produce the precursor.

Freeze granulation

$Fe(NO_3)_3$ and $Al(NO_3)_3$ (produced from $Fe(NO_3)_3{\cdot}9H_2O$ and $Al(NO_3)_3{\cdot}9H_2O$, respectively) were fully dissolved in the deionized water and then sprayed into a liquid nitrogen with drastic stirring to prepare granules. The granular products were then introduced into a freezer for drying at −50 °C and 10 Pa for 12 h to obtain a tawny granule. The granule was then dried at 60 °C for 2 h in a vacuum oven to remove the residual water. Following that, the dried granule was rapidly heated to 300 °C and kept for 4 h in a muffle furnace for the precursor generation.

Calcination

All of the dried precursors were calcinated in a muffle furnace to enhance the mechanical strength of OC particles. The calcination procedure for each precursor is similar. The dried precursor was divided into four parts and firstly calcinated at 900 °C. After 6 h, the first part of the samples was taken out and ground as an OC product. The residual samples were continuously

DOI: 10.1002/apj

calcinated at 1000 °C for another 6 h to obtain the second OC product. The third (calcinated at 1100 °C for another 6 h, the total calcination duration is 18 h at three different temperatures) and fourth OC products (calcinated under 1200 °C for another 6 h, the total calcination time is 24 h at four different temperatures) were obtained in a similar way. Depending on the differences of preparation methods, calcination temperatures, and calcination hours, 28 types of Fe_2O_3/Al_2O_3 (60 wt% : 40wt %) OC particles were produced, which were summarized in Table 1.

COMPARISON AND EVALUATION OF THE PREPARATION TECHNIQUES

Productivity

The OC productivity (ξ), which is defined as the ratio of the finally obtained OC mass to the design mass, was introduced to quantify the production efficiency in the OC preparation process. The productivity for different preparation methods were listed in Table 2, in which the low heat solid reaction and the mechanical mixing techniques lead to the lower productivity due to a larger amount of mass loss in the solid-phase particle synthesis methods. Actually, certain amount of solid reagents was lost during the grinding process in the low heat solid reaction method, and in the mechanical mixing method, the wet gel may conglutinate on the ball surface, resulting in mass loss. Comparatively, in the liquid-phase synthesis methods (e.g. sol-gel, co-precipitation, hydrothermal synthesis, combustion synthesis, and freeze granulation methods), the OC productivities are all higher than 0.7. Therefore, the liquid-phase methods should be considered first in the practical preparation to obtain more OC particles each batch. Still, it should be noted that higher productivity and easier procedure are expected in the solid-phase methods for large-scale OC preparation.

Crushing strength

In the CLC system, OC particles must circulate between the AR and the FR. It thus requires that the OC particles must be rigid enough to resist attrition and fragmentation. In this work, the attrition resistance was reflected by the crushing strength of the OC particle, which was estimated by the peak force when a particle was crushed (tested by a dynamometer, SHIMPO FGJ-5). All particles from different preparation techniques were respectively sieved into two diameter ranges, i.e. $d = 0.125$–0.180 mm and $d > 0.180$ mm. Eight particles were randomly selected (four from $d = 0.125$–0.180 mm

Table 1. Classification of the Fe_2O_3/Al_2O_3 (60 wt% : 40 wt%) oxygen carriers.

Oxygen carrier type	Preparation method	Final sintering temperature (°C)	Total sintering time (h)
SG900C6H	Sol-gel	900	6
SG1000C12H	Sol-gel	1000	12
SG1100C18H	Sol-gel	1100	18
SG1200C24H	Sol-gel	1200	24
CP900C6H	Co-precipitation	900	6
CP1000C12H	Co-precipitation	1000	12
CP1100C18H	Co-precipitation	1100	18
CP1200C24H	Co-precipitation	1200	24
LH900C6H	Low heat solid reaction	900	6
LH1000C12H	Low heat solid reaction	1000	12
LH1100C18H	Low heat solid reaction	1100	18
LH1200C24H	Low heat solid reaction	1200	24
HS900C6H	Hydrothermal synthesis	900	6
HS1000C12H	Hydrothermal synthesis	1000	12
HS1100C18H	Hydrothermal synthesis	1100	18
HS1200C24H	Hydrothermal synthesis	1200	24
MM900C6H	Mechanical mixing	900	6
MM1000C12H	Mechanical mixing	1000	12
MM1100C18H	Mechanical mixing	1100	18
MM1200C24H	Mechanical mixing	1200	24
CS900C6H	Combustion synthesis	900	6
CS1000C12H	Combustion synthesis	1000	12
CS1100C18H	Combustion synthesis	1100	18
CS1200C24H	Combustion synthesis	1200	24
FG900C6H	Freeze granulation	900	6
FG1000C12H	Freeze granulation	1000	12
FG1100C18H	Freeze granulation	1100	18
FG1200C24H	Freeze granulation	1200	24

DOI: 10.1002/apj

Table 2. Productivity of oxygen carriers by various methods.

	Sol-gel	Co-precipitation	Hydrothermal synthesis	Freeze granulation	Low heat solid reaction	Mechanical mixing	Combustion synthesis
ξ (%)	92.99	87.27	71.44	79.18	56.96	53.08	86.35

and the others from $d > 0.180$ mm) and then crushed by the dynamometer (meanwhile the crushing strength was recorded). The average crushing strength of the eight particles was used to represent the rigidity of the OC.

The crushing strength for the different OCs was listed in Table 3, which increases as the calcination temperature and the calcination duration increase. However, the increasing tendency is not very obvious because the calcination temperature of 900 °C may be high enough for particle rigidification. We also found that the crushing strength of these OC particles (which are prepared by the same method and calcinated at the same temperature but for different hours) is almost same (these experimental data are not shown here because of the space limitation). It suggests that the calcination temperature rather than the calcination duration is a crucial influencing factor on the OC crushing strength.

As estimated, the OC crushing strength should be higher than 1 N when used in the CLC system.[39] However, the crushing strength of the OC particles from the low heat solid reaction and hydrothermal synthesis methods are both beyond the reach of 1 N. The OC from liquid-phase synthesis methods, including sol-gel, co-precipitation, combustion synthesis, and freeze granulation, has a higher crushing strength than 1 N, which is suitable for using in the CLC.

In fact, the particle size distribution is also an influencing factor on the performance of oxygen carriers.[40] Therefore, the particle size of all the oxygen carriers is fixed at the same range, 0.125–0.18 mm, to minimize its influence among different techniques. Nevertheless, this work is mainly focused on the effects of preparation techniques on the performance of oxygen carrier. The size distributions of the particles were not paid special attention.

Crystalline phase analysis

The OCs derived by sol-gel, co-precipitation, freeze granulation, mechanical mixing, and combustion synthesis methods were further tested in an X-ray diffraction (XRD) analyzer to determine their crystalline composition. About 1 g particles were characterized by a SHIMADZU XRD-7000 instrument with Cu rake under $2\theta = 10°–90°$, whose maximum tube voltage and current are 40 kV and 30 mA, respectively. The patterns of all samples were similar to that of the sol-gel-derived OC (as presented in Fig. 1), and the main phases in the calcinated particles were Fe_2O_3 and Al_2O_3. When the calcination temperature is 900 °C, OC particles from

Table 3. Crushing strength of oxygen carriers prepared through various techniques.

Sol-gel	SG900C6H	SG1000C12H	SG1100C18H	SG1200C24H
Crushing force (N)	1.34 ± 0.33	1.37 ± 0.25	1.35 ± 0.23	1.39 ± 0.24
Co-precipitation	CP900C6H	CP1000C12H	CP1100C18H	CP1200C24H
Crushing force (N)	1.53 ± 0.50	1.48 ± 0.19	1.60 ± 0.41	1.67 ± 0.55
Low heat solid reaction	LH900C6H	LH1000C12H	LH1100C18H	LH1200C24H
Crushing force (N)	0.70 ± 0.25	0.80 ± 0.20	0.47 ± 0.16	0.80 ± 0.41
Hydrothermal synthesis	HS900C6H	HS1000C12H	HS1100C18H	HS1200C24H
Crushing force (N)	0.95 ± 0.23	0.81 ± 0.33	0.95 ± 0.33	0.99 ± 0.35
Mechanical mixing	MM900C6H	MM1000C12H	MM1100C18H	MM1200C24H
Crushing force (N)	0.96 ± 0.18	0.98 ± 0.11	1.01 ± 0.15	1.33 ± 0.29
Combustion synthesis	CS900C6H	CS1000C12H	CS1100C18H	CS1200C24H
Crushing force (N)	1.06 ± 0.30	1.06 ± 0.29	1.10 ± 0.42	1.11 ± 0.47
Freeze granulation	FG900C6H	FG1000C12H	FG1100C18H	FG1200C24H
Crushing force (N)	1.08 ± 0.17	1.10 ± 0.20	1.17 ± 0.33	1.20 ± 0.22

DOI: 10.1002/apj

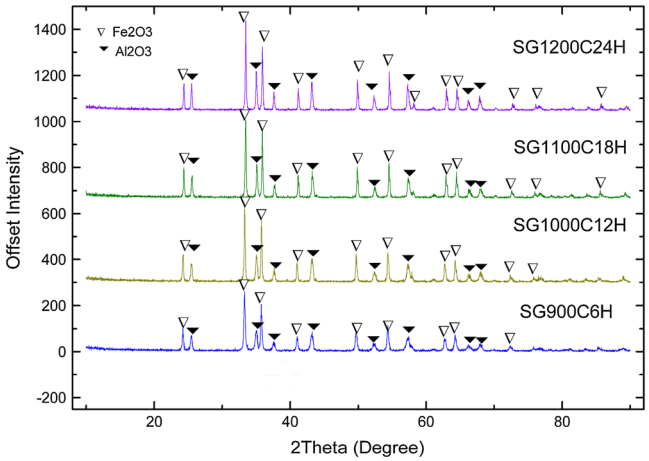

Figure 1. X-ray diffraction patterns of sol-gel-derived oxygen carrier. This figure is available in colour online at www.apjChemEng.com.

different techniques have crystallized. As shown in Fig. 1, the intensity of Al_2O_3 phase is weak in the patterns, indicating that only a small amount of Al_2O_3 phase was formed at this temperature. However, the Fe_2O_3 phase can be clearly detected in the OCs, which indicates that the Fe_2O_3 phase emerges earlier than the Al_2O_3 phase as the calcination temperature increases. We also checked carefully three typical peaks of the XRD patterns of the OC particles calcinated at 900–1100 °C, as shown in Fig. 2. It is clear that the intensity of both Fe_2O_3 and Al_2O_3 phases increases as the calcination temperature increases.

Screening all XRD patterns of these OC particles, we found that the proper temperature for the Al_2O_3 phase formation should be higher than 1000 °C for the co-precipitation, freeze granulation, and sol-gel technologies but higher than 1100 °C for the mechanical mixing and combustion synthesis techniques. It seems that a higher temperature is better for the Al_2O_3 phase formation. In order to verify the conjecture further, we compared the XRD patterns of the OC particles calcinated at 1200 °C (presented in Fig. 3) with those calcinated at lower temperatures (presented in Fig. 1). It is obvious that the intensity of the Al_2O_3 phase in high-temperature-calcinated OC is higher than that calcinated at lower than 1000 °C. Therefore, a higher but reasonable temperature (too high temperature might lead to particle sintering and agglomeration) should be considered in the Al_2O_3-loaded OC preparation. Also as shown in Fig. 3, the OC prepared by the combustion synthesis method has the highest Fe_2O_3 phase intensity, and the co-precipitation and the sol-gel-derived OCs have the second highest intensity. It demonstrates that the combustion synthesis process is positive to the crystalline growth of the Fe_2O_3 phase.

Higher crystallization degree and crystallite dimension are advantageous to better physicochemical properties, such as better mechanical strength, better friction tolerance, and more steady reaction activity.[41] So, it is significant to explore the effect of temperature on the crystallization process. As mentioned earlier, the calcination temperature is one of the crucial influencing factors on the crystalline structure. To explore the temperature-dependent effect, the grain structure parameters and the phase composition were quantified using the XRD-pattern-fitting analysis. The crystallization degree is defined as the percentage of the crystallization area in that of the whole diffraction patterns. The results are shown in Table 4. It was found that the calcination temperature is positive to the crystallization process and a higher temperature leads to a higher crystallization degree. The crystallization degree is less than 90% when the temperature is 900 °C but more than 96% when it is higher than 1100 °C for the co-precipitation, mechanical mixing, combustion synthesis, and freeze granulation methods. We thus concluded that the high temperature calcination is advantageous to the Fe_2O_3/Al_2O_3 crystallization. The calcination temperature has apparent effect on the crystallite dimension (which was estimated by the Scherrer formula[42]) as well. We observed from Table 4 that a higher temperature leads to a larger crystallite dimension. Phase content in the crystalline was estimated by the peak intensity of each phase, which was listed in Table 4. The results showed that the

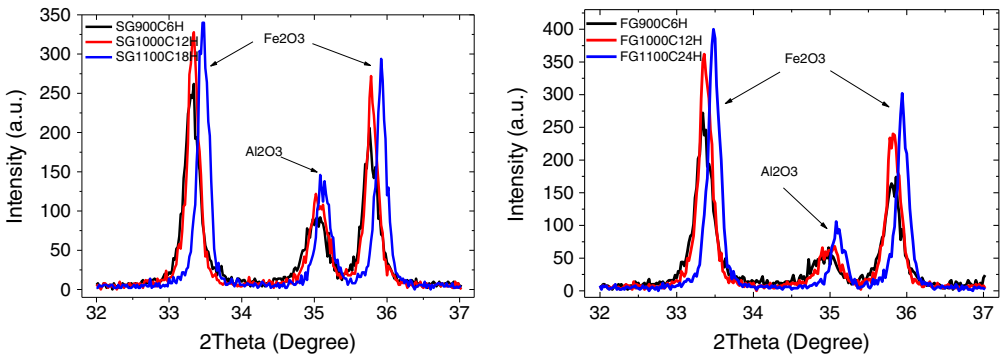

Figure 2. The effect of temperature on the peak intensity. This figure is available in colour online at www.apjChemEng.com.

DOI: 10.1002/apj

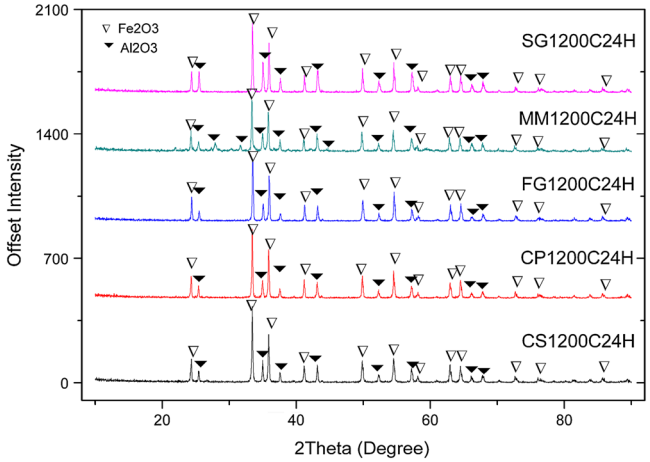

Figure 3. X-ray diffraction patterns of different oxygen carriers. This figure is available in colour online at www.apjChemEng.com.

Fe_2O_3 phase content reduces and the Al_2O_3 phase content increases as the calcination temperature increases. If one expects a good phase composition and a good grain structure in the OC, a high but reasonable calcination temperature should be applied in the calcination process. Based on these considerations, the calcination temperature was suggested as 1200 °C, at which no agglomeration was found.

Reactivity with hydrogen

In order to examine the chemical reactivity of the Fe_2O_3/Al_2O_3 OC prepared by different methods, TPR experiments were performed using a chemisorption analyzer (AutoChemΠ 2920, Micromeritics Co.). A stream of gas containing 10% hydrogen in argon flowed through a U-shape quartz tube containing 200 mg of OC particles at a rate of 50 mL/min. The temperature of the tube was raised from ambient to 1000 °C at a rate of 10 °C/min (maintaining the final temperature for 20 min). Meanwhile, the off-gas was first led to a cold trap to remove the steam and then to a thermal conductivity detector (TCD). The TCD was used to analyze the gas leaving the oxygen carrier. In the TPR experiments, Fe_2O_3/Al_2O_3 OCs derived from five preparation methods (signed as SG1200C24H, CP1200C24H, MM1200C24H, CS1200C24H, and FG1200C24H) were tested.

Figure 4 shows TPR profiles for different OCs, where the TCD signals can be transformed to the hydrogen consumption through the following equation:

$$V_t = A_t F_c \tag{1}$$

where V_t (cm^3) is the hydrogen consumption volume within the period of 0–t, A_t the peak area in the same period, and F_c a constant coefficient. Based on Eqn (1), the hydrogen conversion at time t can be calculated through the following equation:

$$X_{H_2} = \frac{V_t}{V_{total}} \tag{2}$$

where V_{total} (cm^3) is the volume of hydrogen consumed in the whole reaction. Accordingly, the hydrogen conversion rate can be estimated by dX_{H_2}/dt.

Table 4. Results of X-ray diffraction phase analysis.

Method and sample	SG900C6H	SG1000C12H	SG1100C18H	SG1200C24H
Fe_2O_3 (wt%)	100	63.40	71.79	54.50
Degree of crystallization (%)	93.01	96.61	96.90	98.00
Crystallite size (nm)	52.10	57.90	75.90	76.00
Method and sample	CP900C6H	CP1000C12H	CP1100C18H	CP1200C24H
Fe_2O_3 (wt%)	100	86.51	89.53	83.49
Degree of crystallization (%)	89.39	96.93	98.74	98.97
Crystallite size (nm)	51.40	66.40	90.80	68.70
Method and sample	MM900C6H	MM1000C12H	MM1100C18H	MM1200C24H
Fe_2O_3 (wt%)	100	100	100	70.86
Degree of crystallization (%)	85.33	89.59	97.12	98.05
Crystallite size (nm)	37.70	44.60	68.70	70.40
Method and sample	CS900C6H	CS1000C12H	CS1100C18H	CS1200C24H
Fe_2O_3 (wt%)	100	100	78.10	86.68
Degree of crystallization (%)	82.31	87.55	97.20	98.79
Crystallite size (nm)	65.00	72.20	88.40	108.90
Method and sample	FG900C6H	FG1000C12H	FG1100C18H	FG1200C24H
Fe_2O_3 (wt%)	100	74.70	99.35	61.40
Degree of crystallization (%)	88.03	92.72	98.07	98.45
Crystallite size (nm)	39.20	66.00	96.90	110.70

DOI: 10.1002/apj

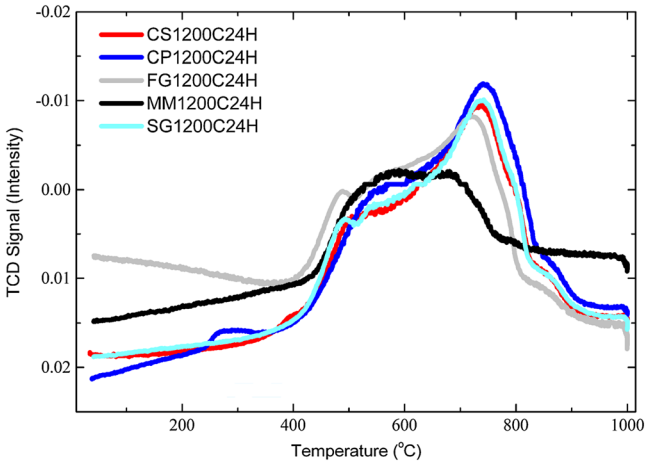

Figure 4. Temperature programmed reduction profiles for different oxygen carriers. This figure is available in colour online at www.apjChemEng.com.

As shown in Fig. 4, the TCD profiles for different OCs demonstrated similar shape with the same peak numbers and approximated peak temperatures (about 780 °C), expect those of mechanical-mixing-derived OC. The characteristic temperature (t_m) corresponding to the maximum hydrogen conversion rate could be determined by differentiating the TCD profiles in Fig. 4. t_m for different OCs was in the range of 795–830 °C. Figure 5 presents the hydrogen conversion rate as a function of the hydrogen conversion for different OCs. Comparing with other samples, FG1200C24H leads to the fastest hydrogen conversion, which is followed by SG1200C24H and CS1200C24H OCs. On the other hand, MM1200C24H and CP1200C24H OCs perform slower conversions, which means that the mechanical-mixing- and co-precipitation-derived OCs cannot remove hydrogen more quickly in the iG-CLC processes. Hence, the OCs derived by freeze granulation, sol-gel, and combustion synthesis are more promising for the iG-CLC from the viewpoint of chemical reactivity.

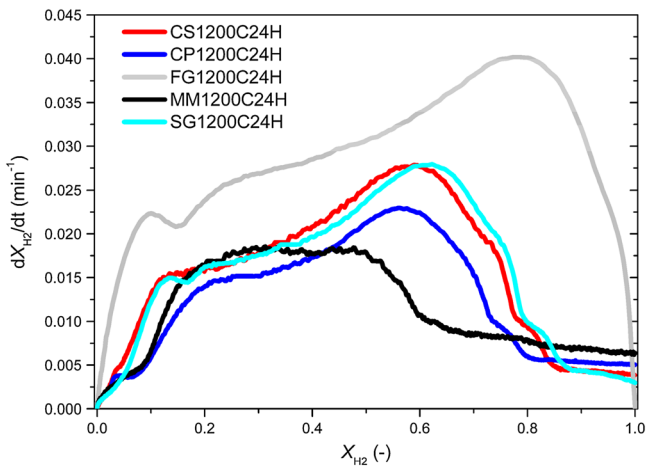

Figure 5. The changing of dX_{H_2}/dt with X_{H_2}. This figure is available in colour online at www.apjChemEng.com.

We also examined the potential cyclic stability of the SG1200C24H particles by carrying out successive TPR–oxidation cycles in the chemisorption analyzer. It was found that the TCD profiles of the ten redox processes are nearly the same, meaning the reactivity of the OC particles keeps well with the increase of the cycle number.

Morphological structure

The Brunauer–Emmett–Teller (BET) surface area of the Fe_2O_3/Al_2O_3 OC particles was evaluated by the N_2-absorption method (Micromeritics, ASAP2020). The BET area of OC particles under different calcination temperatures demonstrates similar tendency. A higher calcinations temperature results in a lower BET surface area. For example, the BET area of SG1100C18H is 2.36 m^2/g, while that of SG1200C24H is 1.39 m^2/g. The shape and morphology of SG1200C24H, CS1200C24H, and FG1200C24H were further studied with environmental scanning electron microscopy. Figure 6(a) shows the microstructure of SG1200C24H, in which the grain size is smaller than 1 μm with slight sintering. However, the sintering is clear in the OC derived by freeze granulation (Fig. 6(b)), and the grain size is larger than 2 μm. It illustrates that the OC from sol-gel has a better anti-sintering property than that from freeze granulation. In addition, we noticed that the sintering in the OCs derived by combustion synthesis (Fig. 6(c)) and sol-gel is similar, which indicates that the two preparation methods are more resistant to particle sintering than the freeze granulation method. However, the OC particles derived by combustion synthesis are not uniform on grain size distribution compared with sol-gel-derived OCs, indicating that the sol-gel method is more appropriate for OC particle preparation. These phenomena are involved with the preparation methods themselves. The sol-gel method was designed based on homogeneous reaction idea, in which the precursor was prepared by a homodisperse process. Although in the combustion synthesis method the gel generation was a homogeneous process as well, the combustion process was drastic and rapid, making the grain grow quickly with a non-uniform distribution. In the freeze granulation method, water in the Fe–Al mixture was quickly removed by the liquid nitrogen, which leads to a lower sintering temperature as a result of probable change of molecular structure during the fast water-removing process. Therefore, the sol-gel method was recommended for the preparation of homogeneous and sintering-resistant Fe_2O_3/Al_2O_3 OCs.

DOI: 10.1002/apj

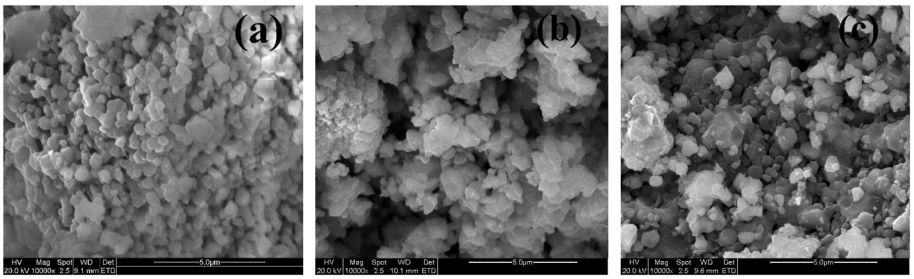

Figure 6. Environmental scanning electron microscopy graphs of SG1200C24H (a), CS1200C24H (b), and FG1200C24H (c).

Finally, based on the comprehensive physico-chemical characterization and measurements for the Fe_2O_3/Al_2O_3 OCs, the sol-gel and freeze granulation methods were preferred for laboratory-scale OC preparation, and the optimal calcination temperature was selected as 1200 °C. However, we also noted here the freeze granulated particles did not show good fuel conversion[43] in CLC units, whereas impregnated particles on Al_2O_3 allow complete combustion of gases,[44] being resistant to sulfur.[45]

REACTION KINETICS OF THE SOL-GEL-DERIVED FE_2O_3/AL_2O_3 WITH HYDROGEN

In the iG-CLC process, the coal gasification is a rate-limiting step. However, it can be accelerated by removing H_2 (generated in the gasification) quickly through the reduction reaction with the OC. Therefore, the reaction between the Fe_2O_3/Al_2O_3 OC and H_2 is worth of investigation. This section focused on its reduction kinetics and mechanism. We concentrated on the sol-gel-derived Fe_2O_3/Al_2O_3 OC calcinated at 1200 °C (signed as SG1200C24H). TPR experiments were performed at different heating rates ($\beta = 5$, 7, 10, 13, 15, 18, 21 °C/min).

Oxygen carrier conversion

The mass-based OC conversion was calculated by the following equation:

$$X = \frac{m_{ox} - m}{m_{ox} - m_{red}} \quad (3)$$

where m_{ox} (g) is the mass of the OC when fully oxidized and m_{red} (g) is the mass of the OC in complete reduction form. $(m_{ox} - m)$ is equal to the oxygen consumption within 0–t, and $(m_{ox} - m_{red})$ is equal to the oxygen consumption within the whole reduction. According to the reaction equation $H_2 + O \rightarrow H_2O$, the oxygen consumptions within 0–t and the whole reduction are equal to the corresponding hydrogen consumptions. It means that the OC conversion X is equal to the hydrogen conversion XH_2.

The use of alumina as support allows the formation of iron aluminate as the reduction state, increasing the oxygen transport capacity of the OC.[24] Our XRD of OC particles after reduction also showed the presence of the mixture of Fe_3O_4 and $FeAl_2O_4$. The reduction of Fe_2O_3 does not follow the sequence Fe_2O_3-Fe_3O_4-FeO-Fe. The sequence in the reduction for particles composed by Fe_2O_3 and Al_2O_3 is Fe_2O_3-Fe_3O_4-$FeAl_2O_4$-Fe. Moreover, thermodynamic calculations by HSC software showed that by using iron-based OCs supported on alumina, it is possible to reach full combustion of H_2 and CO into H_2O and CO_2 when Fe_3O_4 and/or $FeAl_2O_4$ are formed. Further reduction to wustite (FeO) or Fe would produce a high decrease in the CO_2 purity obtained in the FR because of the increase in the equilibrium concentrations of CO and H_2. Therefore, the Fe_2O_3 should be reduced as maximum to a mixture of Fe_3O_4 and $FeAl_2O_4$ in order to obtain full fuel gas combustion in a CLC system.

The TCD patterns under different heating rates are similar to that displayed in Fig. 4. The two peaks in the TCD signal correspond to two reactions (R1) and (R2) in the TPR process. Theoretically, the critical temperature between the two reactions is 380 °C from the thermodynamic simulation of HSC software; however, the actual transition temperature was about 600 °C (as shown in Fig. 4). Accordingly, the hydrogen conversion patterns were divided into two segments by the temperature 600 °C. On the other side, the hydrogen consumption in (R2) is two times of that in (R1), which means that $X = 0.33$ is a critical point for the two reactions. As a result, the conversion patterns, as shown in Fig. 7, can be further divided into two segments by the conversion 0.33. No obvious effect of temperature ramp rate has been observed for this subject. Taking into consideration the actual transition temperature and the critical conversation, the hydrogen conversion patterns were divided into two segments as follows.

Segment I. Temperature 25–600 °C; OC conversion $X = 0$–0.35;

$$\text{Reaction : } H_2(g) + 3Fe_2O_3 \rightarrow 2Fe_3O_4 + H_2O(g) \quad (R1)$$

DOI: 10.1002/apj

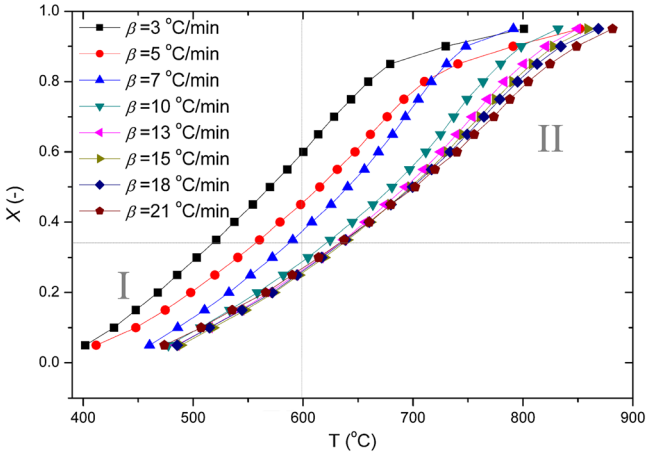

Figure 7. Oxygen carrier conversion under different heating rates. This figure is available in colour online at www.apjChemEng.com.

Segment II. Temperature 600–1000 °C; OC conversion $X = 0.35$–0.95;

$$\text{Reaction}: H_2(g) + Fe_3O_4 + 3Al_2O_3 \rightarrow 3FeAl_2O_4 + H_2O(g) \quad \text{(R2)}$$

In the following analysis, we respectively analyzed the reaction mechanisms and kinetics of the two stages using the non-isothermal kinetics analysis and the double extrapolation method.[46] The conversion of each stage were generalized to the range of 0–1. For the two stages, the different signs were used to represent the OC conversion: X^{I} represents the OC conversion in stage I and X^{II} in stage II. The OC conversion for each stage was then used to confirm the respective activation energy (E, kJ/mol), pre-exponential factor (A, s^{-1}), reaction order (n), and mechanism function ($G(X)$).

Mechanism and kinetics analysis for the two stages

Generally, two kinds of methods can be used to determine the mechanism, i.e. the differential method and the integral method. Because a bigger error might arise in the differential process,[46] we utilized the integral method to study the reduction kinetics in this work. The widely used kinetic equations in the integral method are Eqns (4.1)–(4.3), in which $G(X)$ is the integral form of mechanism function (partly listed in Table 5), A is the pre-exponential factor, β (K/min) represents the heating rate, T_0 and T (K) refer respectively to the start and the end temperatures of the reaction, E (kJ/mol) the activation energy, and R (kJ/(mol·°C)) the gas constant.

$$\text{Arrhenius function}: k(T) = A\exp\left(-\frac{E}{RT}\right) \tag{4.1}$$

$$\text{Kinetic equation}: \frac{dX}{dt} = k(T)f(X) \tag{4.2}$$

$$\text{Integral form}: G(X) = \int_0^X \frac{dX}{f(X)} = \frac{A}{\beta}\int_{T_0}^{T} \exp\left(-\frac{E}{RT}\right)dT = k(T)t \tag{4.3}$$

After variables separation and integration, Eqn (4.3) leads to

$$G(X) = \frac{A}{\beta}\left[\int_0^T \exp\left(-\frac{E}{RT}\right)dT - \int_0^{T_0} \exp\left(-\frac{E}{RT}\right)dT\right] \tag{4.4}$$

Further, using the same procedure as Tian *et al.*,[36] Eqn (4.4) was transferred to

$$\ln F(X,E,T) = \ln\frac{G(X)}{T^2Q(u)\left\{1 - \left(\frac{T_0}{T}\right)^2\frac{Q(u_0)}{Q(u)}\exp[-(u_0-u)]\right\}} = \ln\frac{AR}{\beta E} - \frac{E}{RT} \tag{5}$$

where $u = E/RT$, and $Q(u)$ is expressed as

$$Q(u) = \frac{\int_u^\infty y^{-2}\exp(-y)dy}{u^{-2}\exp(-u)} \tag{6}$$

$Q(u)$ was further approximated by Chen *et al.*[47] to the following formula with quite high accuracy:

Table 5. Part of the generally used kinetics mechanism functions.

Reaction model	$G(X)$
Jander function	$[1-(1-X)^{1/2}]^n$ ($n = 1/2, 2$)
Z–L–T function	$[(1+X)^{-1/3}-1]^2$
Avrami–Erofeev	$[-\ln(1-X)]^n$ ($n = 1/4, 1/3, 2/5, 1/2, 2/3, 3/4, 1, 3/2, 2, 3, 4$)
P–T function	$\ln[(1-X)/X]$
Mampel	X^n ($n = 1/4, 1/3, 1/2, 1, 3/2, 2$)
	$1-(1-X)^n$ ($n = 1/4, 1/3, 1/2, 2, 3, 4$)
	$(1-X)^{-n}$ ($n = 1, 1/2$)
Index law	$\ln X^n$ ($n = 1, 2$)

DOI: 10.1002/apj

$$Q(u) = \frac{3u^2 + 16u + 4}{3u^2 + 22u + 30} \quad (7)$$

When taking the (X, T) values from TPR experiments into Eqn (5) under a certain β (signed as β_1), the linear correlation coefficient r between $\ln F(X, E, T)$ and $1/T$ was obtained. In our calculation, the frequently used 40 different reaction mechanism functions $G(X)$ (Table 5) were examined one by one to identify $G(X)$ candidates with good linear relation ($|r| > 0.99$). For each $G(X)$, the corresponding activation energy $E_{\beta 1}$ and the pre-exponential factor $A_{\beta 1}$ can be obtained by regression analysis. The similar procedures were adopted for other heating rates to identify their $G(X)$ candidates that lead to a very high linear relation between $\ln F(X, E, T)$ and $1/T$. Then, the mechanism functions $G(X)$ with good linear factor r close to 1 (e.g. $|r| > 0.99$) for all the eight heating rates were determined. The values of the kinetic parameters with heating rate close to zero, $E_{\beta \to 0}$, and $\ln A_{\beta \to 0}$, for every screened function were gained when the heating rate was extrapolated to zero.

The value of activation energy can be achieved directly using the Ozawa equation (Eqn (8)),[48] even though the reaction mechanism function is not yet known. For a given reaction, the $G(X)$ is fixed, indicating that the values of $G(X)$, E, and A are constant under a certain X. Under this condition, $\lg\beta$ has a linear relation with $1/T$ (Eqn (8)); thus, the activation energy E_X under this conversion can be determined. After screening the other X, the E_X under all the conversions can be obtained. By extrapolating X to zero, the activation energy $E_{X \to 0}$ can be estimated.

$$\lg\beta = \lg\left[\frac{AE}{RG(X)}\right] - 2.315 - 0.4567\frac{E}{RT} \quad (8)$$

The last step was to compare $E_{\beta \to 0}$ with $E_{X \to 0}$ one by one. The $G(X)$ that leads to the smallest difference between $E_{\beta \to 0}$ and $E_{X \to 0}$ was determined as the most probable mechanism function.

For the first-stage reduction, the linear relation of $\ln F(X, E, T)$ and $1/T$ was directly used to determine the mechanism function because only one $G(X)$ can lead to the best linear relation for all heating rates. As displayed in Table 6, the mechanism function $G(X) = (1 - X)^{-1} - 1$ leads to the best linear relation between $\ln F(X, E, T)$ and $1/T$ under different β, which was confirmed as the most probable mechanism function for the first-stage reduction. This $G(X)$ is a surface reaction model, which means H_2 adsorbs on the Fe_2O_3 surface and reacts with it, and then Fe_3O_4 is generated and the resultant gaseous H_2O is then desorbed from the OC surface. The differential form of the $G(X)$ is $f(X) = (1 - X)^2$, so the conversion rate is described by $dX/dt = k(T)(1 - X)^2$, and the maximum power of X is 2, which is at the same time the reaction order. The E_X^{I} under different X^{I} was shown in Fig. 8, in which the activation energy decreases with the increasing of the conversion X^{I}. This phenomenon occurs because there is no active site on the surface of the particles under a low temperature at the very start of the reduction. The activation energy is reduced under higher temperatures because of the emergence of more active sites. When X^{I} was extrapolated to zero, the activation energy is $E_{X \to 0}^{\mathrm{I}} = 125.4$ kJ/mol, and the logarithm of the pre-exponential factor is $\ln A_{X \to 0}^{\mathrm{I}} = 16.3\ \mathrm{s}^{-1}$.

With respect to the second-stage reduction, Fe_3O_4 was further reduced to $FeAl_2O_4$. The mechanism function was determined by the double extrapolation method. By using the Ozawa equation, the values of E_X^{II} (in the range of 85–110 kJ/mol) were obtained.

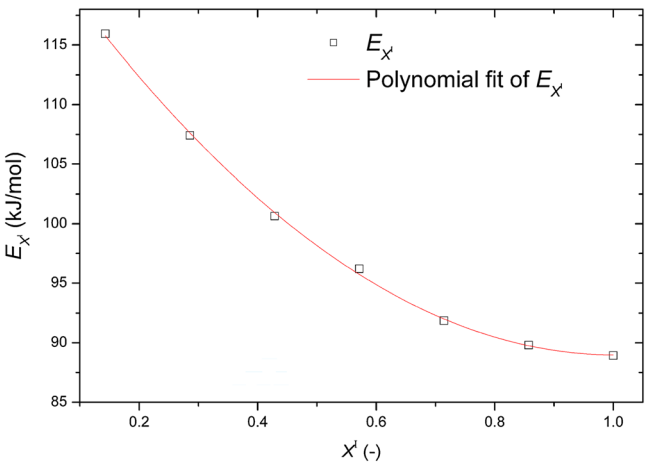

Figure 8. Effects of oxygen carrier conversion on the activation energy in the first stage. This figure is available in colour online at www.apjChemEng.com.

Table 6. The mechanism functions with higher linear factors in the first stage.

	$\beta = 5$ °C/min			$\beta = 7$ °C/min			$\beta = 10$ °C/min		
$G(X)$	E	$\ln A$	r	E	$\ln A$	r	E	$\ln A$	r
$-\ln(1 - X)$	18.058	2.127	0.995	43.799	3.653	0.991	39.342	2.930	0.992
$[-\ln(1 - X)]^{3/2}$	17.192	6.206	0.995	43.474	8.509	0.991	39.155	7.321	0.992
$[-\ln(1 - X)]^4$	16.369	26.800	0.996	43.271	32.853	0.991	39.165	29.319	0.991
$(1 - X)^{-1} - 1$	10.608	3.087	0.999	35.199	4.923	0.996	35.213	4.280	0.997

DOI: 10.1002/apj

As presented in Fig. 9, E_X^{II} increases as X^{II} increases. When X^{II} was extrapolated to zero, the value of $E_{X\to 0}^{II}$ is estimated as 87.1 kJ/mol. Afterward, Eqn (5) is employed to find the mechanism functions $G(X)$ that give good linear relation between $\ln F(X, E, T)$ and $1/T$ and to obtain the corresponding activation energy E_β and pre-exponential factor A_β. The results showed that the following five mechanism functions, i.e. $G(X) = [(1+X)^{-1/3} - 1]^2$, $G(X) = [-\ln(1-X)]^4$, $G(X) = [-\ln(1-X)]^{1/2}$, $G(X) = [-\ln(1-X)]^{3/4}$, and $G(X) = [-\ln(1-X)]^{1/3}$, lead to good linear relation ($|r| > 0.99$). The corresponding E_β of each $G(X)$ decreases with the increase of the heating rate, as shown in Fig. 10. The most probable mechanism function was determined as $G(X) = [-\ln(1-X)]^{3/4}$ because its $E_{\beta\to 0}$ (88.4 kJ/mol) approximates nearly to $E_{X\to 0}^{II}$ (87.1 kJ/mol). The mechanism function represents a nucleation and nuclei growth model. This means that in the reaction between Fe_3O_4 and H_2, the Fe–O bond is broken first, generating $FeAl_2O_4$ with Al_2O_3 and gaseous product H_2O. The generated $FeAl_2O_4$ then diffuses away from the reduction centers and agglomerates together to form $FeAl_2O_4$ molecular clusters. Finally, the $FeAl_2O_4$ clusters coalesce to form $FeAl_2O_4$ crystallites. The activation energy $E_{X\to 0}^{II}$ and the logarithm of the pre-exponential factor $\ln A_{X\to 0}^{II}$ are 87.1 kJ/mol and 15.3 s^{-1}, respectively.

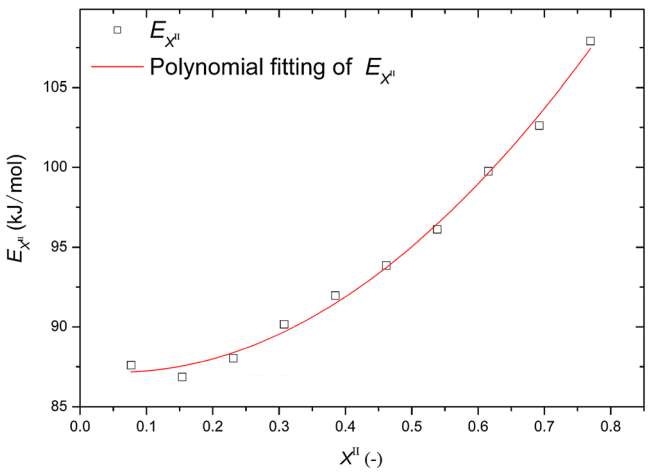

Figure 9. The activation E_X^{II} changing with X^{II}. This figure is available in colour online at www.apjChemEng.com.

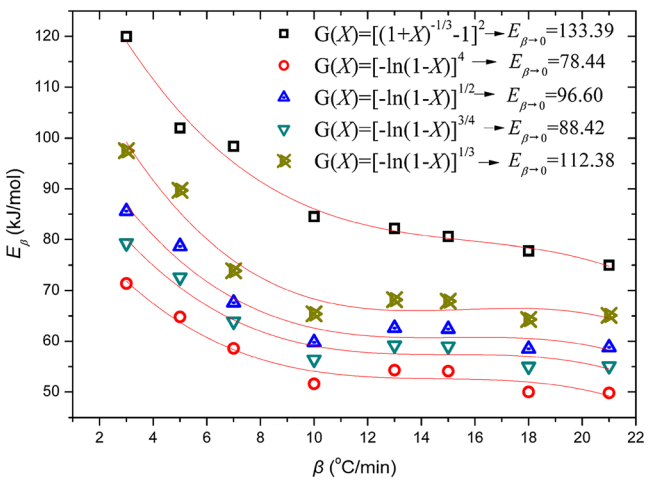

Figure 10. The activation E_β changing with β. This figure is available in colour online at www.apjChemEng.com.

CONCLUSIONS

In this paper, a commonly used Fe_2O_3/Al_2O_3 OC for CLC was prepared by seven methods. A comprehensive physicochemical characterization was carried out to investigate the effects of preparation techniques on the OC performance. In the comparison of the preparation methods, the liquid-phase methods, such as sol-gel, co-precipitation, hydrothermal synthesis, freeze granulation, and combustion synthesis, showed higher Fe_2O_3/Al_2O_3 OC productivities. They should be given priority for the OC preparation. The crushing strength measurements illustrated that a higher temperature leads to a higher crushing strength and the preparation technique also has influence on the crushing strength of the OC. The OCs derived by the low heat solid reaction and hydrothermal synthesis methods have a crushing strength lower than 1 N, which is not hard enough for using in the CLC system. A high calcination temperature is advantageous to the growth of Fe_2O_3 and Al_2O_3 crystalline. The temperature impact on growth of the Fe_2O_3 crystalline is more evident than that on Al_2O_3, that is, the Fe_2O_3 crystalline grows earlier than the Al_2O_3 crystalline as the calcination temperature increases. For the formation of Al_2O_3 phase, the calcination temperature was confirmed as 1200 °C. Calcination duration has no evident influence on the OC properties. The reactivity tests of the OCs calcinated at 1200 °C showed that the OCs derived by freeze granulation, combustion synthesis, and sol-gel perform faster hydrogen conversion and better reactivity than others. Among them, the OCs derived by freeze granulation lead to the fastest hydrogen conversion rate. However, environmental scanning electron microscopy measurements indicated that the sol-gel-derived OC exhibits more homogeneous morphological structure than that derived by the other two methods. Taking into consideration various physicochemical indices, the sol-gel and freeze granulation methods were preferred for OC preparation.

The kinetics and mechanism of reduction reaction between the sol-gel-derived Fe_2O_3/Al_2O_3 and H_2 were further investigated through the non-isothermal kinetics analysis and the double extrapolation method. The conversion of the sol-gel-derived Fe_2O_3/Al_2O_3 in the reduction reaction by H_2 can be divided into two

DOI: 10.1002/apj

stages. For the first-stage reduction, Fe_2O_3 is converted to Fe_3O_4, which can be described by the chemical reaction model $G(X) = (1-X)^{-1} - 1$ with an order of 2, indicating that the reaction between H_2 and Fe_2O_3 is controlled by a surface reaction process. Hydrogen first adsorbs on the OC surface and reacts with the active component Fe_2O_3, generating Fe_3O_4 and gaseous H_2O, which is then desorbed from the OC surface. The activation energy $E_{X\to 0}^{\mathrm{I}}$ and the pre-exponential factor $\ln A_{X\to 0}^{\mathrm{I}}$ are 125.4 kJ/mol and 16.3 s^{-1}, respectively. For the second-stage reduction, Fe_3O_4 is further reduced to $FeAl_2O_4$ in a nucleation and nuclei growth mode, which means that the Fe–O bond in Fe_3O_4 is broken in the reaction with H_2, generating $FeAl_2O_4$ molecule and gaseous H_2O. Once generated, the $FeAl_2O_4$ molecule diffuses away from the active centers and agglomerates together to form $FeAl_2O_4$ clusters. Finally, the clusters grow to form $FeAl_2O_4$ crystal. The mechanism function for the second stage is $G(X) = [-\ln(1-X)]^{3/4}$. The activation energy $E_{X\to 0}^{\mathrm{II}}$ and the pre-exponential factor $\ln A_{X\to 0}^{\mathrm{II}}$ are 87.1 kJ/mol and 15.3 s^{-1}, respectively.

Acknowledgements

The authors were supported by the National Natural Science Foundation of China (51390494) and the National Key Basic Research and Development Program (2011CB707300). Meanwhile, the staff from the Analytical and Testing Center, Huazhong University of Science and Technology, are also appreciated for the related experimental analysis.

REFERENCES

[1] N. Ding, Y. Zheng, C. Luo, Q. Wu, P. Fu, C. Zheng. *Chem. Eng. J.*, **2011**; *171*, 1018–1026.
[2] H. Zhao, L. Liu, B. Wang, D. Xu, L. Jiang, C. Zheng. *Energy Fuels*, **2008**; *22*, 898–905.
[3] M.M. Hossain, H.I. Lasa. *AIChE J.*, **2007**; *53*, 1817–1829.
[4] T. Mattisson, A. Järdnäs, A. Lyngfelt. *Energy Fuels*, **2003**; *17*, 643–651.
[5] B.M. Corbella, L.F. Diego, F. García-Labiano, J. Adánez, J. M. Palacios. *Environ. Sci. Technol.*, **2005**; *39*, 5796–5803.
[6] L. Shen, J. Wu, Z. Gao, J. Xiao. *Combust. Flame*, **2009**; *156*, 1377–1385.
[7] L.F. Diego, F. García-Labiano, J. Adánez, P. Gayán, A. Abad, B.M. Corbella, J.M. Palacios. *Fuel*, **2004**; *83*, 1749–1757.
[8] S.Y. Chuang, J.S. Dennis, A.N. Hayhurst, S.A. Scott. *Combust. Flame*, **2008**; *154*, 109–121.
[9] A. Lambert, C. Delquié, I. Clémençon, E. Comte, V. Lefebvre, J. Rousseau, B. Durand. *Energy Procedia*, **2009**; *1*, 375–381.
[10] Z. Sun, L. Liu, D. Jia, W. Pan. *Sens. Actuators B*, **2007**; *125*, 144–148.
[11] M. Rydén, E. Cleverstam, M. Johansson, A. Lyngfelt, T. Mattisson. *AIChE J.*, **2010**; *56*, 2211–2220.
[12] M. Johansson, T. Mattisson, A. Lyngfelt. *Ind. Eng. Chem. Res.*, **2004**; *43*, 6978–6987.
[13] P. Cho, T. Mattisson, A. Lyngfelt. *Fuel*, **2004**; *83*, 1215–1225.
[14] P. Erri, A. Varma. *Chem. Eng. Sci.*, **2007**; *62*, 5682–5687.
[15] P. Erri, A. Varma. *Ind. Eng. Chem. Res.*, **2006**; *46*, 8597–8601.
[16] P. Erri, A. Varma. *Ind. Eng. Chem. Res.*, **2009**; *448*, 4–6.
[17] J. Adánez, L.F. Diego, F. García-Labiano, P. Gayán, A. Abad, J.M. Palacios. *Energy Fuels*, **2004**; *18*, 371–377.
[18] K. Go, S. Son, S. Kim. *Int. J. Hydrogen Energy*, **2008**; *33*, 5986–5995.
[19] S. Wang, G. Wang, F. Jiang, M. Luo, H. Li. *Energ. Environl. Sci.*, **2010**; *3*, 1353–1360.
[20] M.M. Hossain, H.I. de Lasa. *Chem. Eng. Sci.*, **2008**; *63*, 4433–4451.
[21] J. Adanez, A. Abad, F. Garcia-Labiano, P. Gayan, L.F. De Diego. *Prog. Energ. Combust. Sci.*, **2012**; *38*, 215–282.
[22] I. Adánez-Rubio, P. Gayán, F. García-Labiano, L.F. Diego, J. Adánez, A. Abad. *Energy Procedia*, **2011**; *4*, 417–424.
[23] A. Abad, F. García-Labiano, L.F. Diego, P. Gayán, J. Adánez. *Energy Fuels*, **2007**; *21*, 1843–1853.
[24] A.M. Kierzkowska, C.D. Bohn, S.A. Scott, J.P. Cleeton, J.S. Dennis, C.R. Müller. *Ind. Eng. Chem. Res.*, **2010**; *49*, 5383–5391.
[25] L.F. de Diego, F. Garcia-Labiano, J. Adanez, P. Gayan, A. Abad, B.M. Corbella, J. Maria Palacios. *Fuel*, **2004**; *83*(13), 1749–1757.
[26] M. Keller, H. Leion, T. Mattisson, A. Lyngfelt. *Combust. Flame*, **2011**; *158*, 393–400.
[27] S.A. Scott, J.S. Dennis, A.N. Hayhurst, T. Brown. *AIChE J.*, **2006**; *52*, 3325–3328.
[28] F. Garcia-Labiano, L.F. de Diego, P. Gayan, A. Abad, J. Adanez. *Chem. Eng. Sci.*, **2013**; *87*, 173–182.
[29] P. Markstrom, C. Linderholm, A. Lyngfelt. *Chem. Eng. Sci.*, **2013**; *96*, 131–141.
[30] J.T. Richardson, B. Turk, M.V. Twigg. *Appl. Catal., A*, **1996**; *148*, 97–112.
[31] B. Moghtaderi, H. Song. *Energy Fuels*, **2010**; *24*, 5359–5368.
[32] S. Vyazovkin, C.A. Wight. *Int. Rev. Phys. Chem.*, **1998**; *17*, 407–433.
[33] M. Avrami. *J. Chem. Phys.*, **1939**; *7*, 1103–1112.
[34] M. Avrami. *J. Chem. Phys.*, **1941**; *9*, 177–184.
[35] M.M. Hossain, M.R. Quddus, H.I. Lasa. *Ind. Eng. Chem. Res.*, **2010**; *49*, 11009–11017.
[36] H. Tian, Q. Guo, J. Chang. *Energy Fuels*, **2008**; *22*, 3915–3921.
[37] A. Abad, J. Adánez, A. Cuadrat, F. García-Labiano, P. Gayán, L.F. Diego. *Chem. Eng. Sci.*, **2011**; *66*, 689–702.
[38] F. García-Labiano, L.F. Diego, J. Adánez, A. Abad, P. Gayán. *Ind. Eng. Chem. Res.*, **2004**; *43*, 8168–8177.
[39] A. Shulman, E. Cleverstam, T. Mattisson, A. Lyngfelt. *Energy Fuels*, **2009**; *23*, 5269–5275.
[40] L.F. de Diego, F. Garcia-Labiano, P. Gayan, J. Celaya, J.M. Palacios, J. Adanez. *Fuel*, **2007**; *86*, 1036–1045.
[41] S. Freiman, L. Hench. *J. Am. Ceram. Soc.*, **1972**; *55*, 86–90.
[42] A. Patterson. *Phys. Rev.*, **1939**; *56*, 978–982.
[43] A. Abad, T. Mattisson, A. Lyngfelt, M. Johansson. *Fuel*, **2007**; *86*, 1021–1035.
[44] P. Gayán, M.A. Pans, M. Ortiz, A. Abad, L.F. de Diego, F. García-Labiano, J. Adánez. *Fuel Process. Technol.*, **2012**; *96*, 37–47.
[45] A. Cabello, C. Dueso, F. García-Labiano, P. Gayán, A. Abad, L.F. de Diego, J. Adánez. *Fuel*, **2014**; *121*, 117–125.
[46] Y. Pan, X. Guan, Z. Feng, X. Li, Y. Wu. *Chin. J. Inorg. Chem.*, **1999**; *15*, 247–251 (In Chinese).
[47] H. Chen, N. Liu. *AIChE J.*, **2006**; *52*, 4181–4185.
[48] T. Ozawa. *J. Therm. Anal.*, **1970**; *2*, 301–324.

DOI: 10.1002/apj